

Simultaneously Enhancing Adsorbed Hydrogen and Dinitrogen to Enable Efficient Electrochemical NH₃ Synthesis on Sm(OH)₃

Zengxiang Lv, Zexu Li, Honghong Liu, Weixiang Li, Tai-Sing Wu, Song Hong, Yukun Ruan, Yun-Liang Soo, Leiduan Hao, Liang Xu, Alex W. Robertson, Pei Xiong, Molly Meng-Jung Li, Liang-Xin Ding,* and Zhenyu Sun*

The electrochemical N₂ reduction reaction (ENRR), driven by renewable electricity and run under ambient conditions, offers a promising sustainable avenue for carbon-neutral NH₃ production. Yet, to efficiently bind and activate the inert N₂ remains challenge. Herein, effective and stable electrochemical NH₃ synthesis on Sm(OH)₃ via enhanced adsorption of hydrogen and dinitrogen by dual integration of sulfur dopants and oxygen vacancies (V_O) is reported. The resulting S-doped lanthanide electrocatalyst attains both a good NH₃ yield rate, exceeding 21 μg_{NH₃} h⁻¹ mg_{cat.}⁻¹, and an NH₃ faradaic efficiency of over 29% at -0.3 V (vs reversible hydrogen electrode) in an H-type cell using a neutral electrolyte, figures of merit that are largely maintained after 2 days of consecutive polarization. Density functional theory calculations show that the adsorption energy barrier of N₂ on S-Sm(OH)₃(V_O) is greatly lowered by the introduction of V_O. In addition, the S sites improve the adsorption of hydrogen produced via the Volmer reaction, which is conducive to the formation of the *N-NH intermediate (i.e., the potential determining step, PDS) on adjacent Sm sites, and thereby significantly promotes the reaction kinetics of ENRR. The PDS free energy for the catalyst is comparable with the values at the peak of the ENRR volcano plots of leading transition metal catalyst surfaces.

1. Introduction

Ammonia (NH₃) is an essential primary feedstock and important intermediate across industry, agriculture, and pharmaceuticals, as well as being an effective hydrogen carrier and a carbon-free fuel. The invention of artificial NH₃ synthesis by reacting gaseous dinitrogen (N₂) and hydrogen (H₂), known as the Haber-Bosch (HB) process, dramatically promoted the growth of the world population.^[1-3] Commercial preparation of NH₃ remains dominated by this century-old HB process and its derivatives (e.g., Fauser, Casale, Claude, NEC, Mont-Cenis), which are energy- and capital-intensive. Current NH₃ production thus requires the burning of a substantial amount of fossil fuels, with an energy consumption of ≈26 GJ t_{NH₃}⁻¹, leading to ≈1.8% of the world's carbon dioxide (CO₂) emissions.^[4-7] The search for environmentally friendly NH₃ synthesis

Z. Lv, Z. Li, W. Li, S. Hong, Y. Ruan, L. Hao, L. Xu, Z. Sun
State Key Laboratory of Organic-Inorganic Composites
Beijing University of Chemical Technology
Beijing 100029, China
E-mail: sunzy@mail.buct.edu.cn

Z. Li
School of Chemistry
Beihang University
Beijing 100191, China


H. Liu, L.-X. Ding
School of Chemistry and Chemical Engineering
South China University of Technology
Guangzhou 510640, China
E-mail: lxding@scut.edu.cn

T.-S. Wu
National Synchrotron Radiation Research Center
Hsinchu 30076, Taiwan

Y.-L. Soo
Department of Physics
National Tsing Hua University
Hsinchu 30013, Taiwan

A. W. Robertson
Department of Physics
University of Warwick
Coventry CV47AL, UK

P. Xiong, M. M. J. Li
Department of Applied Physics
The Hong Kong Polytechnic University
Hong Kong 999077, China

 The ORCID identification number(s) for the author(s) of this article can be found under <https://doi.org/10.1002/sstr.202300158>.

© 2023 The Authors. Small Structures published by Wiley-VCH GmbH. This is an open access article under the terms of the Creative Commons Attribution License, which permits use, distribution and reproduction in any medium, provided the original work is properly cited.

DOI: 10.1002/sstr.202300158

methods has thus emerged as a new theme in catalyst science, as research investment seeks to achieve a sustainable and carbon-neutral future. The electrochemical nitrogen reduction reaction (ENRR) driven by renewable electricity provides a number of favorable characteristics, such as mild reaction conditions, the potential for zero carbon emissions when using water as the hydrogen source, simple operation, compatibility with intermittent power supplies, low capital cost, and relatively higher energy efficiency than the conventional HB process. The ENRR is thus seen as a promising green NH₃ synthesis technology.^[7–12]

Three main pathways have been put forward for NRR to yield NH₃, namely, dissociative, associative, and Mars–van Krevelen mechanisms. In the dissociative pathway, the adsorbed dinitrogen (*N₂, *denotes adsorption sites) first dissociates into nitrogen adatoms (*N) by breaking the N≡N triple bond, which is then hydrogenated to form *NH₃ through *NH and *NH₂ intermediates.^[13] This mechanism is applicable to the NRR performed at high temperatures, which is particularly the case for heterogeneous thermal catalysis. Ambient NRR is generally considered to follow an associative mechanism, which can be classified into two types depending on the pathway of N₂ activation. On the one hand, an N₂ molecule is first adsorbed and hydrogenated (followed by dissociation of the triple bond) in either a distal or an alternating manner to produce two NH₃ molecules.^[14,15] Alternatively, rather than N₂ adsorption, the reduction of H⁺ (to form *H) is considered to be the initial step for catalysts with weak N₂-binding affinities, whereupon the N₂ is subsequently activated and reduced to *N₂H₂ by surface *H, followed by concerted exothermic addition of protons and electrons.^[16] A Mars–van Krevelen mechanism is proposed for the NRR on transition metal nitrides; specifically, the surface nitrogen of the nitrides is first reduced to NH₃, generating nitrogen vacancies, which preferentially act as effective adsorption and activation centers for N₂.^[17]

Activating N₂ at room temperature presents an ongoing challenge due to its extreme stability and inertness, with a large cleavage energy and a huge energy gap between the highest occupied molecular orbital (HOMO) and lowest unoccupied molecular orbital (LUMO). In addition, the NRR suffers from slow reaction kinetics due to demanding the transfer of six electrons, as well as the ubiquitous competition with the parasitic hydrogen evolution reaction (HER) that occurs with more rapid kinetics under similar or even lower overpotentials. Despite the recent encouraging advances that have been achieved in the last 5 years, the NRR is still constrained by issues such as low yield rate and faradaic efficiency (FE) toward NH₃, as well as a large formation overpotential and insufficient stability. Under such circumstances, discovering, designing, and synthesizing efficient electrocatalysts to address these challenges have become a timely subject in the field of ENRR.^[18–22]

To facilitate the NRR, a strong interaction between the catalyst and the N₂ molecule is essential. A “donation” (accepting the lone-pair electrons of a N₂ molecule to decrease its HOMO’s electron density) and “π back-donation” (donating electrons into the antibonding π orbitals of an adsorbed N₂ molecule to enhance its LUMO’s electron density) process is supposed to weaken the N≡N bond for N₂ activation. A range of transition metals with *d*-orbital electrons and *d*-block metals with *p*-orbital electrons

have been reported for efficient nitrogen fixation.^[23–25] However, lanthanide-based metals for ENRR have been rarely explored likely due to the formidable energy cost for N₂ activation. Herein, we designed and synthesized, for the first time, S-doped nanowire-like Sm(OH)₃ rich in oxygen vacancies (V_O), S-Sm(OH)₃(V_O), toward efficient electrocatalytic N₂ fixation under neutral conditions. A synergy is achieved by combining S doping and V_O, affording substantially strengthened N₂ adsorption. In particular, the as-obtained S-Sm(OH)₃(V_O) imparts both an impressive NH₃ yield rate of ≈21.1 μg_{NH₃} h^{−1} mg_{cat.}^{−1} and an NH₃ FE approaching ≈29.2% at −0.3 V (vs reversible hydrogen electrode, vs RHE), outperforming many previously reported transition metal- and noble metal-based materials. Density functional theory (DFT) calculations reveal that the adsorption energy barrier of N₂ on S-Sm(OH)₃(V_O) is lowered upon introducing V_O, and the formation free energy of the *N–NH intermediate is dramatically reduced owing to the enhanced proton transfer after S doping, thereby significantly promoting the reaction kinetics of ENRR. This work provides a new perspective on the design and construction of active and cost-effective electrocatalysts for NH₃ electrosynthesis.

2. Results and Discussion

2.1. Structure and Morphology Analysis

S-doped Sm(OH)₃ nanowires rich in V_O were synthesized through a facile two-step solvothermal method using SmCl₃ and Na₂S·9H₂O as Sm and S precursors, respectively (for details, see the ESI). X-ray diffraction (XRD) measurements (Figure 1a) showed pronounced reflections at around 16.1°, 28°, 29.1°, and 40.8°, which can be well attributed to the (100), (110), (101), and (201) crystal planes of hexagonal Sm(OH)₃, respectively (JCPDS no. 83-2-36).^[26] No shift of the diffraction peaks or additional reflections were discerned for Sm(OH)₃ after S doping, indicating the formation of high-purity Sm(OH)₃ with good crystallinity. The Fourier transform infrared (FTIR) spectra of the samples display two characteristic bands located at ≈698.2 and 3608.2 cm^{−1}, corresponding to the stretching vibration of O–H and the bending vibration of Sm–O–H,^[27] respectively (Figure 1b). The Raman spectra of Sm(OH)₃ and S-Sm(OH)₃(V_O) are shown in Figure S1, Supporting Information. Three major peaks at ≈303.5, 375.5, and 481.6 cm^{−1} were observed, which can be assigned to A_g translatory, E_{2g} translatory, and E_{1g} liberation modes,^[28] respectively.

The surface composition and chemical valence state of the samples were examined by X-ray photoelectron spectroscopy (XPS) (Figure 1c,d and S2–S4, Supporting Information). The two peaks at around ≈1082.5 and ≈1109.3 eV, as illustrated in Figure 1c, originate from Sm 3*d*_{5/2} and Sm 3*d*_{3/2},^[29] respectively. Notably, both peaks shifted toward lower binding energies (BEs) after incorporation of S, indicating more electrons around the Sm due to the lower electronegativity of S (2.5) than O (3.5).^[30] In the S 2*p* XPS spectrum of S-Sm(OH)₃(V_O), the peak with a BE of 161.8 eV arose from S linked with Sm. Meanwhile, a peak with a higher BE at 168.9 eV was also observed (Figure 1d), which was attributed to the positive valence of S.^[31] In contrast, no S signal was detectable for pure Sm(OH)₃. These results

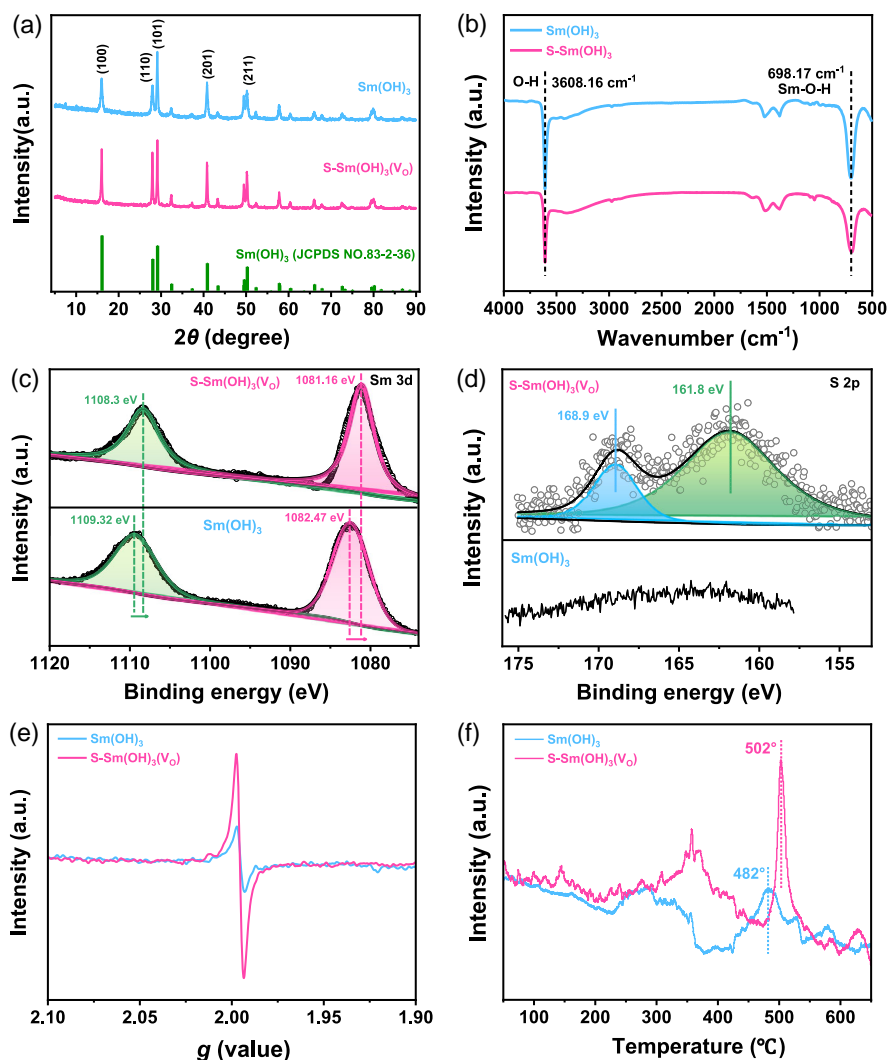


Figure 1. a) XRD patterns, b) FTIR spectra, c) Sm 3d XPS spectra, d) S 2p XPS spectra, e) EPR spectra, and f) N₂-TPD profiles of Sm(OH)₃ and S-Sm(OH)₃(V_O).

suggest the successful doping of S into Sm(OH)₃. It is worth noting that no signals of N were probed for the samples (Figure S2, Supporting Information), ruling out N source interference from the obtained catalysts. The O 1s peak at ≈ 530.8 eV for Sm(OH)₃ stems from lattice oxygen, whereas the peak corresponding to lattice oxygen for S-Sm(OH)₃ shifted to a higher BE (≈ 531.2 eV) (Figure S3, Supporting Information), owing to less electrons around O due to the electronic donation capacity of S being noticeably lower than that of Sm. The surface content of vacancy oxygen in S-Sm(OH)₃(V_O) was derived to be ≈ 0.35, larger than that of Sm(OH)₃ (0.29).

The existence of V_O in both samples was also analyzed by electron paramagnetic resonance (EPR) spectroscopy. Compared to bare Sm(OH)₃, S-Sm(OH)₃(V_O) shows a prominently stronger pair of symmetric peaks, with a signal at *g* = 2.0, confirming the presence of more V_O in S-Sm(OH)₃(V_O) (Figure 1e). A high density of V_O can significantly enhance the adsorption and activation of N₂, thereby facilitating its further conversion.

Nitrogen adsorption–desorption isotherms of Sm(OH)₃ and S-Sm(OH)₃(V_O) both exhibit a type III isotherm (Figure 1f). S-Sm(OH)₃(V_O) delivers a Brunauer–Emmett–Teller (BET) surface area of ≈ 87.7 m² g^{−1} and a total pore volume of ≈ 1.35 cm³ g^{−1}, 5.4 and 12.9 times that of Sm(OH)₃, respectively (Figure S5a,b, Supporting Information). This increase in the specific surface area promotes the adsorption of N₂ and the transport of intermediates, thus favoring the ENRR. N₂ temperature-programmed desorption (N₂-TPD) was employed to probe the N₂ adsorption ability of the samples. As illustrated in the N₂-TPD profiles (Figure 1f), the peaks located at 145 °C are attributed to the physisorption of N₂, while the peaks at 250–400 and 450–550 °C result from the chemisorption of N₂.^[31] Relative to Sm(OH)₃, S-Sm(OH)₃(V_O) exhibits notably stronger signals of chemisorbed N₂ with chemisorption peaks shifting toward higher temperatures. The outstanding N₂ adsorption uptake and high N₂ binding affinity of S-Sm(OH)₃(V_O) are greatly beneficial to the ENRR.

To gain insight into the electronic structure and coordination environment of Sm sites in $\text{Sm}(\text{OH})_3$ and $\text{S-Sm}(\text{OH})_3(\text{V}_\text{O})$, synchrotron X-ray absorption near-edge structure (XANES) and extended X-ray absorption fine structure (EXAFS) analyses were conducted. The Sm L_3 -edge position of $\text{S-Sm}(\text{OH})_3(\text{V}_\text{O})$ and white-line intensity are lower than that of $\text{Sm}(\text{OH})_3$ (Figure 2a), indicating the lower valence state of Sm in $\text{S-Sm}(\text{OH})_3(\text{V}_\text{O})$ compared to $\text{Sm}(\text{OH})_3$ owing to electron transfer from S to Sm. The Fourier transform EXAFS spectrum of $\text{Sm}(\text{OH})_3$ shows a dominant first shell peak at $2.45 \pm 0.01 \text{ \AA}$ (Figure 2b and Table S1, Supporting Information), which can be attributed to the Sm–O^[32] bond with a coordination number (CN) of 9.0 ± 0.7 . While for $\text{S-Sm}(\text{OH})_3$, the first peak can be fitted well using Sm–O with a CN of 7.9 ± 0.6 at $2.47 \pm 0.01 \text{ \AA}$ and Sm–S with a CN of 0.6 ± 0.2 at $2.74 \pm 0.02 \text{ \AA}$ (Figure 2b and Table S1, Supporting Information), demonstrating that S was introduced by replacing O to bond with Sm. In addition, the total CN of the first peak in $\text{S-Sm}(\text{OH})_3(\text{V}_\text{O})$ (≈ 8.5) is less than that in $\text{Sm}(\text{OH})_3$ (≈ 9), which also suggests the presence of more oxygen vacancies in the former sample, agreeing well with our previous XPS results. Furthermore, an enhanced scattering and a stretched Sm–Sm bond at the second shell could be seen in the wavelet transform-EXAFS of $\text{Sm}(\text{OH})_3$ and $\text{S-Sm}(\text{OH})_3(\text{V}_\text{O})$ (Figure 2c,d and Table S1, Supporting Information).

The morphology and microstructure of $\text{S-Sm}(\text{OH})_3(\text{V}_\text{O})$ were examined by scanning electron microscopy (SEM) and

high-angle annular dark-field scanning-mode transmission electron microscopy (HAADF-STEM) along with energy dispersive X-ray spectroscopy (EDS). SEM (Figure 3a) and low-magnification HAADF-STEM observations (Figure 3b) show the wire-like morphology of the obtained sample. The nanowires are uniform with an average length and diameter of approximately $1.2 \mu\text{m}$ and 31.2 nm , respectively. High-magnification STEM images (Figure 3c,d) and fast Fourier transforms (FFT, Figure 3e) reveal the high crystallinity of the nanowires. Ordered interplanar spacing fringes of 0.31 nm were observed (Figure 3c), attributed to the (101) plane of $\text{Sm}(\text{OH})_3$. Interestingly, abundant nanovoids with sizes of about 2 nm were found at the surface of the nanowires (Figure 3b–d). Dislocations and distortions of the lattices (encased with a white dot-dashed square in the inset of Figure 3d) can also be seen.^[33] EDS spectrum (Figure S6, Supporting Information) and elemental mapping display the uniform distribution of S, O, and Sm in the $\text{S-Sm}(\text{OH})_3(\text{V}_\text{O})$ nanowires (Figure 3f–i), validating that S is successfully introduced into the sample and is homogeneously dispersed throughout the nanowires.

2.2. ENRR Investigation

The ENRR catalytic properties of the as-synthesized $\text{S-Sm}(\text{OH})_3(\text{V}_\text{O})$ were investigated using an H-type cell with a Nafion 117 membrane in $0.1 \text{ M Na}_2\text{SO}_4$ solution at room temperature and atmospheric pressure. The feed gas N_2 was

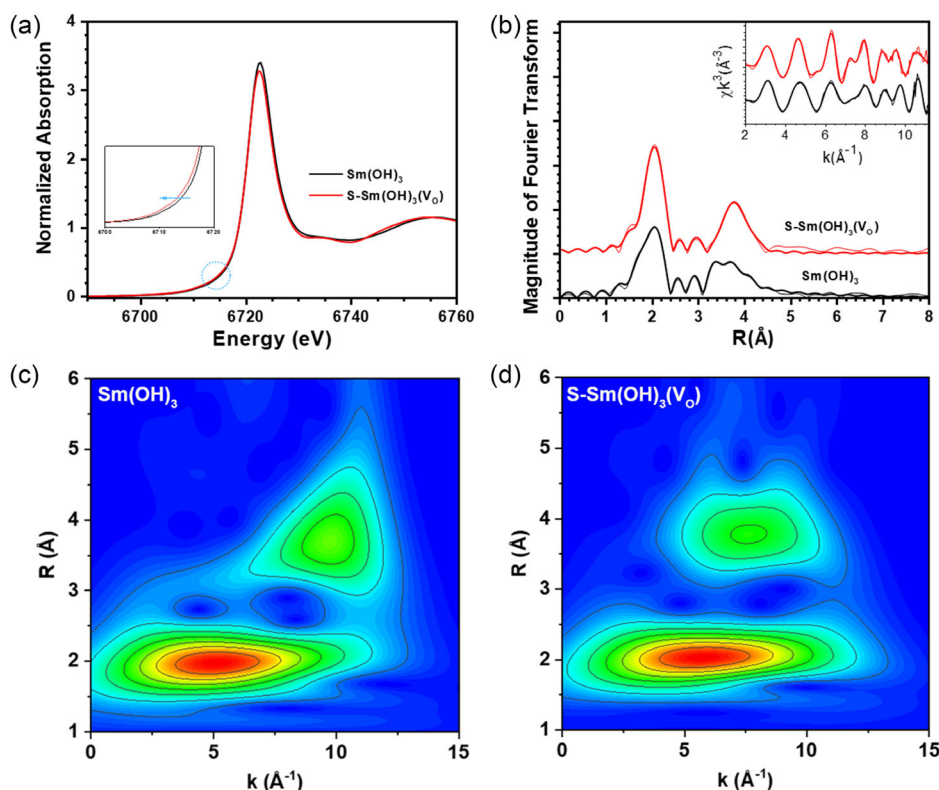


Figure 2. a) Normalized XANES spectra of $\text{Sm}(\text{OH})_3$ and $\text{S-Sm}(\text{OH})_3(\text{V}_\text{O})$ at the Sm L_3 -edge. b) Fourier transform EXAFS spectra at the k^3 -weighted L_3 -edges of $\text{Sm}(\text{OH})_3$ and $\text{S-Sm}(\text{OH})_3(\text{V}_\text{O})$. The inset shows the $\text{Sm}(\text{OH})_3$ and $\text{S-Sm}(\text{OH})_3(\text{V}_\text{O})$ raw EXAFS function. Wavelet transform for the k^3 -weighted EXAFS spectra of c) $\text{Sm}(\text{OH})_3$ and d) $\text{S-Sm}(\text{OH})_3(\text{V}_\text{O})$.

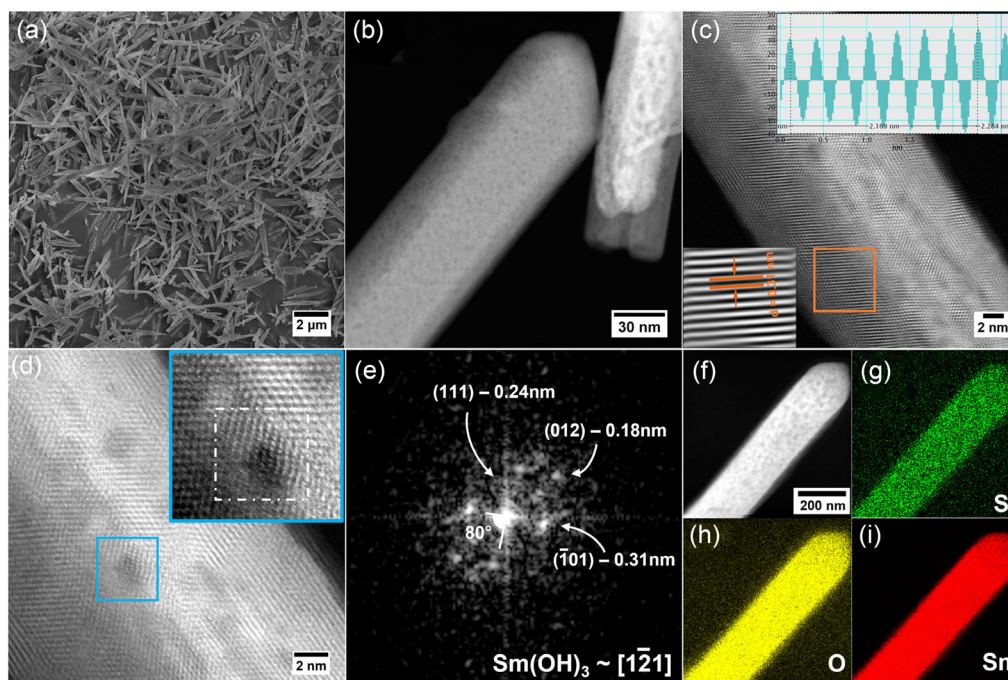


Figure 3. a) SEM image, b) low- and c,d) high-magnification HAADF-STEM images of S-Sm(OH)₃(VO). Top inset in (c): diagram of lattice spacing. Bottom inset in (c): magnified view of the region encased by the orange square. Inset in (d): magnified view of the area encased by the blue square. e) FFT of the regime denoted by the blue square in (d). f–i) STEM image and corresponding EDS elemental maps of S, O, and Sm for S-Sm(OH)₃(VO).

continuously bubbled into the cathodic chamber throughout the ENRR process. The potentials reported in this work refer to the RHE scale. To exclude the false positive results caused by external NH₃ and nitrogen-containing species (e.g., NO_x, NO₂⁻, and NO₃⁻), all the experimental conditions were strictly controlled prior to the ENRR tests. Specifically, the H-cell devices and membranes were subjected to ultrasonication with 0.05 M H₂SO₄ and deionized H₂O for 15 min, respectively. The carbon papers used for the ENRR were ultrasonicated with anhydrous ethanol and deionized H₂O for 15 min, respectively. The feeding gas N₂ was prepurified with 1 M FeSO₄, 1 M NaOH, and 1 M H₂SO₄, respectively, to eliminate any possible presence of NO, NO₂, and NH₃ species before introducing into the electrolyte. The bottles used during the tests were cleaned with pure ethanol under bath ultrasonication, and further washed at least 3 times with deionized H₂O. High-purity electrolytes were selected and no NO₂⁻ and NO₃⁻ contaminants were identified in the electrolytes, as presented in Figure S7–S9, Supporting Information.

The ENRR activities of the samples were first evaluated by linear sweep voltammetry (LSV) in Ar and N₂-saturated 0.1 M Na₂SO₄. As shown in Figure S10, Supporting Information, Sm(OH)₃ and S-Sm(OH)₃(VO) both show a small current density in Ar-purged electrolyte. In stark contrast, a substantial increase in current density was observed in N₂-saturated electrolyte, implying the occurrence of ENRR. Notably, S-Sm(OH)₃(VO) exhibited a distinctly higher reduction current than neat Sm(OH)₃, signifying its superior response to ENRR. We further analyzed the ENRR performance by chronovoltammetry tests for 1 h between -0.1 and -0.5 V with a potential interval of 0.1 V. The amount of NH₃ generated in electrolytes was estimated

through an indophenol blue method (Figure S11, Supporting Information). The by-product N₂H₄ was undetectable by the Watt and Chrisp method^[34] within the applied potential range (Figure S12 and S13, Supporting Information). Also, no NO₂⁻ and NO₃⁻ were identified, ruling out the occurrence of oxidation of nitrogen to NO_x by OH. These reflect the good selectivity of S-Sm(OH)₃(VO) for NH₃. Evidently, S-Sm(OH)₃(VO) outperforms bare Sm(OH)₃ in terms of both production rate (r_{NH_3}) and FE toward NH₃ formation (Figure 4a,b). A r_{NH_3} as high as 21.14 μg_{NH₃} h⁻¹ mg_{cat.}⁻¹ was achieved at -0.3 V on S-Sm(OH)₃(VO), about 2 times that of pure Sm(OH)₃ (r_{NH_3} : 10.02 μg_{NH₃} h⁻¹ mg_{cat.}⁻¹). The NH₃ FE reached up to ≈29.2%, which is also higher than that of pure Sm(OH)₃ (25.6%), also exceeding many prior reported metal-based electrocatalysts (Table S2, Supporting Information). Almost no NH₃ was identified on the bare carbon paper electrodes, suggesting that the ENRR was initiated by Sm(OH)₃.

To ensure the validity and reliability of our experiment results, ¹H nuclear magnetic resonance (¹H NMR) (Figure S14, Supporting Information) and ammonium ion selective electrode (ISE) (Figure S15 and S16, Supporting Information) were also utilized to quantify the yield of NH₃. Both NMR and ISE results were almost identical to the value derived by the indophenol blue method (Figure 4b). To investigate the influence of light on indophenol blue method, the electrolytes were incubated by indophenol blue method in dark condition and visible light condition, respectively. It could be observed that the light had no profound effect on the accuracy of indophenol dye (Figure S17, Supporting Information), indicating the authenticity of our quantification results. The plots of overall cathodic reduction current density

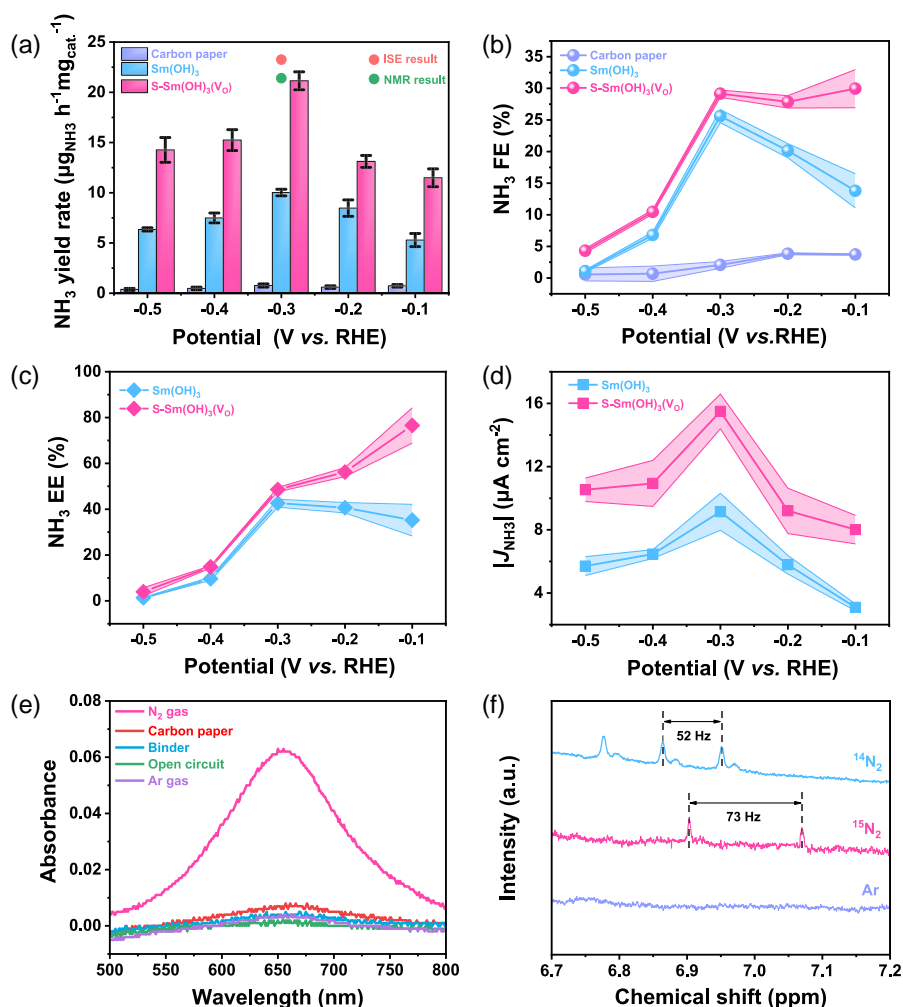


Figure 4. a) NH_3 yield rate, b) NH_3 FE, c) NH_3 EE, and d) absolute NH_3 partial geometric current density as a function of applied potential for various working electrodes. e) UV-vis spectra of the electrolytes (catholyte and anolyte) after 1 h of electrolysis at -0.3 V in either N_2 -(N_2 gas) or Ar-purged electrolyte (Ar gas), or at an open circuit potential (open circuit), or with the Nafion binder solution (binder), or without catalyst (carbon paper). f) ^1H NMR spectra of the electrolytes after electrolysis with $^{14}\text{N}_2$, $^{15}\text{N}_2$, or Ar as the feed gas.

and NH_3 partial current density against applied potential are given in Figure S18, Supporting Information and Figure 4d, respectively. It can be seen that both the total current density and NH_3 partial current density of S-Sm(OH) $_3$ (V $_O$) exceed those of Sm(OH) $_3$ in the voltage range from -0.1 to -0.5 V. The maximum NH_3 partial geometric current density of S-Sm(OH) $_3$ (V $_O$) is $15.5 \mu\text{A cm}^{-2}$, 1.7 times that of pure Sm(OH) $_3$ ($9.1 \mu\text{A cm}^{-2}$). Meanwhile, the energy conversion efficiency toward NH_3 (EE) was calculated and plotted versus applied potential, as illustrated in Figure 4c. Likewise, S-Sm(OH) $_3$ (V $_O$) affords a larger EE value than that of Sm(OH) $_3$ across the voltage window, reaching 48.5% at -0.3 V.

To check the origin of NH_3 production, a multitude of blank and control experiments as well as $^{15}\text{N}_2$ isotope measurements were carried out. As shown in Figure 4e, only traces of NH_3 were detected in Ar-saturated electrolyte, on bare carbon paper in the absence of S-Sm(OH) $_3$ (V $_O$), with the Nafion binder solution, or at an open circuit potential. This rules out the source of NH_3 being

from the Ar, electrolyte, carbon paper, catalyst, or contaminants from the surrounding environment, and supports that the NH_3 obtained here originated from reduction of N_2 . We also performed the ENRR using a higher purity N_2 feed gas (99.9999%, Figure S19, Supporting Information). Similar NH_3 formation rate and FE were obtained (Figure S20, Supporting Information), suggesting that the minor impurities in N_2 with purity $\geq 99.9999\%$ here unlikely influence the ENRR results. Isotope labeling experiments using a $^{15}\text{N}_2$ feed gas with ^1H NMR were further conducted. Doublet peaks with a coupling constant of ≈ 73 Hz were observed for the product with $^{15}\text{N}_2$ supply in accord with the standard signals of $^{15}\text{NH}_4^+$. This contrasts to triplet peaks with a coupling constant of ≈ 52 Hz for the product with $^{14}\text{N}_2$ feed gas corresponding to $^{14}\text{NH}_4^+$ (Figure 4f). No peaks assigned to $^{14}\text{NH}_4^+$ and $^{15}\text{NH}_4^+$ were discerned when Ar was used as a feed gas. Note that the synthesis of S-Sm(OH) $_3$ (V $_O$) does not involve nitrogen-containing precursors or solvents. Indeed, there is no detectable N species in the as-obtained

samples, as corroborated by XPS measurements (Figure S2, Supporting Information). The above results hence strongly suggest that the detected NH_3 arose from the ENRR rather than ambient pollutants.

To examine the stability of the catalyst, alternating electrolysis experiments between N_2 - and Ar-saturated electrolytes were performed. Almost no NH_3 was detected for all the three cycles in Ar-saturated electrolyte (Figure 5a and S21 and S22, Supporting Information). This suggests the evolution of NH_3 must occur from the N_2 reactant. It is worth noting that the NH_3 yield remained stable over six alternating cycles. Additionally, the overall current density, r_{NH_3} , and NH_3 FE of $\text{S-Sm}(\text{OH})_3(\text{V}_\text{O})$ were essentially constant for ten independent electrochemical experiments (Figure S23 and S24, Supporting Information), indicating excellent reproducibility of N_2 electrolysis on $\text{S-Sm}(\text{OH})_3(\text{V}_\text{O})$. Moreover, chronoamperometric measurements were carried out to evaluate the long-term durability of the catalyst. Strikingly, the current density remained almost unchanged even after 55 h of continuous ENRR (Figure 5b). In addition, over 93% of the original NH_3 yield rate and 88% of NH_3 FE were preserved after the prolonged electrolysis cycle (the inset of Figure 5b and S25, Supporting Information). Postcharacterization of the catalyst after electrolysis by XRD showed identical peaks with the original sample (Figure S26, Supporting Information), affirming its good structural durability. Furthermore, the surface valence state of Sm, S, and O was well retained (Figure S27, Supporting Information). Inductively coupled plasma optical emission spectrometry (ICP-OES) test was also performed after 55 h of continuous ENRR. No apparent leaching of Sm was identified, confirming good stability of the $\text{S-Sm}(\text{OH})_3(\text{V}_\text{O})$ during

the long electrocatalysis (Table S3, Supporting Information). These aspects unambiguously demonstrate the good recycling capability, outstanding activity, and exceptional stability of the $\text{S-Sm}(\text{OH})_3(\text{V}_\text{O})$.

Tafel plot and electrochemical impedance spectroscopy (EIS) were analyzed to investigate the intrinsic electrochemical activities of the catalysts.^[35] The Tafel slope is $175.58 \text{ mV dec}^{-1}$ for $\text{S-Sm}(\text{OH})_3(\text{V}_\text{O})$, much less than $\text{Sm}(\text{OH})_3$ ($275.5 \text{ mV dec}^{-1}$), suggesting the more rapid reaction kinetics of $\text{S-Sm}(\text{OH})_3(\text{V}_\text{O})$ (Figure 5c). EIS measurements showed that $\text{S-Sm}(\text{OH})_3(\text{V}_\text{O})$ possesses a lower resistance and higher electron transfer efficiency than pristine $\text{Sm}(\text{OH})_3$, benefiting the ENRR (Figure S28, Supporting Information). Further operando Raman measurements display a peak at $\approx 1590 \text{ cm}^{-1}$ corresponding to the N–H stretching mode, which became stronger with the extension of electrolysis time from 10 to 30 min (Figure 5d).^[36] This indicates occurrence of ENRR under the reaction conditions.

2.3. Mechanistic Understanding of ENRR

To further understand the intrinsic mechanisms of enhanced ENRR performance on $\text{S-Sm}(\text{OH})_3(\text{V}_\text{O})$, we conducted DFT calculations. Based on the above XRD and XAFS results, we considered the (101) facet of hexagonal $\text{Sm}(\text{OH})_3$. The $\text{S-Sm}(\text{OH})_3(\text{V}_\text{O})$ was modeled by substituting one O atom with an S atom (Figure 6a). V_O was also taken into account by removing an O atom next to the Sm atom. We first calculated the alternating and distal pathways of ENRR on $\text{Sm}(\text{OH})_3$ and $\text{S-Sm}(\text{OH})_3(\text{V}_\text{O})$ to identify the lowest free energy route. The formation of $^*\text{N-NH}$ intermediates ($^*\text{N}_2 + (\text{H}^+ + \text{e}^-) \rightarrow ^*\text{N-NH}$) was found to be the

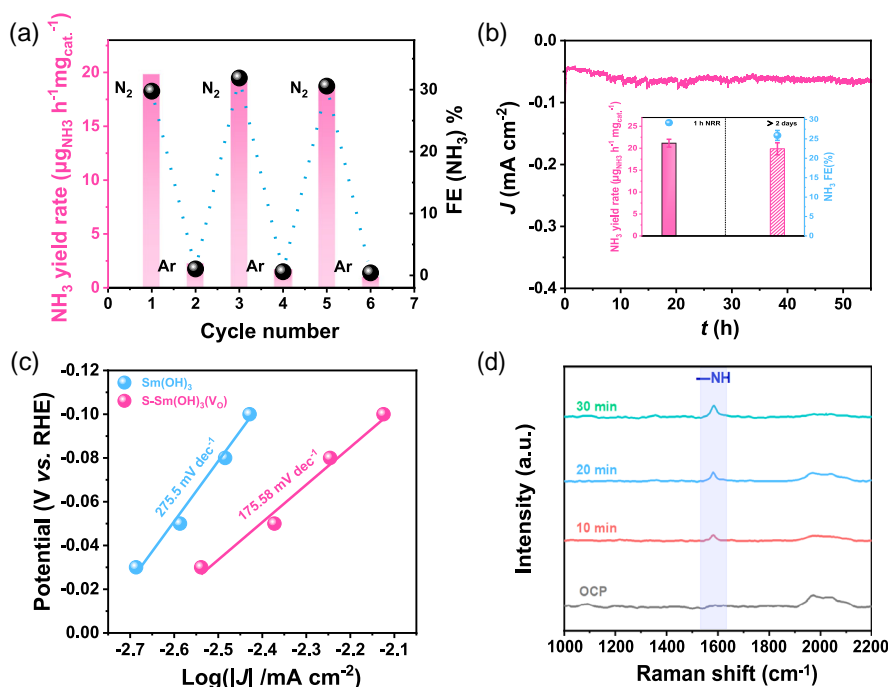


Figure 5. a) NH_3 yield rate (bar) and FE (ball) with alternated Ar and N_2 cycles under -0.3 V over $\text{S-Sm}(\text{OH})_3(\text{V}_\text{O})$. b) Chronoamperometric stability test at -0.3 V on $\text{S-Sm}(\text{OH})_3(\text{V}_\text{O})$ in N_2 -saturated $0.1 \text{ M Na}_2\text{SO}_4$. The inset shows the NH_3 yield rate and NH_3 FE after 1 and 55 h of N_2 electrolysis at -0.3 V on $\text{S-Sm}(\text{OH})_3(\text{V}_\text{O})$. c) Tafel plots for NH_3 production of $\text{Sm}(\text{OH})_3$ and $\text{S-Sm}(\text{OH})_3(\text{V}_\text{O})$. d) Operando Raman spectra of $\text{S-Sm}(\text{OH})_3(\text{V}_\text{O})$ against electrolysis time at -0.3 V .

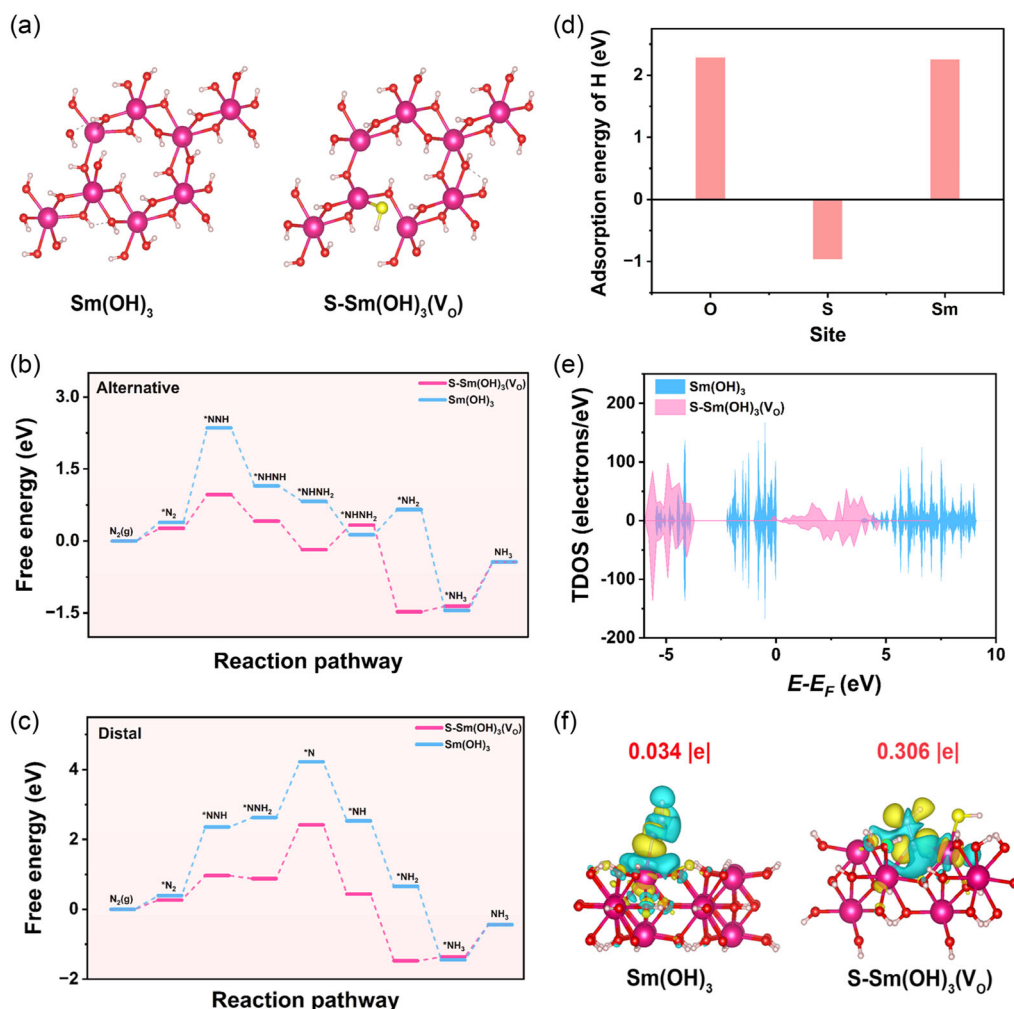


Figure 6. a) DFT calculation models of Sm(OH)₃ and S-Sm(OH)₃(V_O). Gibbs free energy diagrams of NRR on Sm(OH)₃ and S-Sm(OH)₃(V_O) via b) an alternating pathway and c) a distal pathway. d) The adsorption energy of H on the O and Sm sites of Sm(OH)₃ and S sites of S-Sm(OH)₃(V_O). e) TDOS of Sm(OH)₃ and S-Sm(OH)₃(V_O). f) The difference of electron density of *N-NH intermediates adsorbed on Sm(OH)₃ and S-Sm(OH)₃(V_O). Yellow and blue isosurfaces in (f) are presented as positive and negative charges of density, respectively.

potential-determining step (PDS) (i.e., the largest free energy requiring electrochemical step) for both catalysts in the alternating path (Figure 6b). The free energy of *N-NH formation is thus a reasonable descriptor for ENRR activity, which is substantially lowered on S-Sm(OH)₃(V_O) (0.7 eV) compared with that on pure Sm(OH)₃ (1.96 eV). This qualitatively agrees with the experimental results that S-Sm(OH)₃(V_O) is more active than Sm(OH)₃ for ENRR. We note that the free energy change at PDS on S-Sm(OH)₃(V_O) (0.7 eV) is comparable with the values (≈ 1.0 eV) at the top of the NRR volcanoes on various transition metal surfaces.^[37] Next, we obtained a free energy diagram for ENRR via the distal pathway (Figure 6c), in which the PDS for Sm(OH)₃ is the generation of *N-NH species, as found for the alternating pathway. However, for S-Sm(OH)₃(V_O), the first *NH₃ desorption (1.54 eV) requires a much higher free energy than the *N-NH formation, which is therefore regarded as the PDS. In light of the observation that the free energy of PDS in the alternating mechanism is much lower than that demanded

in the distal pathway, it is inferred that the ENRR tends to proceed through an alternating pathway on S-Sm(OH)₃(V_O).^[38] Moreover, we calculated the free energies of N₂ adsorption on the surfaces of Sm(OH)₃, Sm(OH)₃(V_O), and S-Sm(OH)₃(V_O), which are 0.398, 0.251, and 0.263 eV, respectively (Figure S29, Supporting Information). This indicates that the introduction of V_O favored enhancement of N₂ adsorption, which in turn facilitates the subsequent ENRR.

To investigate the role of S sites on the reaction pathway (Figure S30, Supporting Information), the adsorption energy of H was calculated. As shown in Figure 6d, the adsorption of H on the O and Sm sites of Sm(OH)₃ is an endothermic process with a free energy as high as 2.28 and 2.25 eV, respectively, denoting difficult adsorption of H on the O and Sm sites. In contrast, the adsorption of H occurs readily on the S sites in S-Sm(OH)₃(V_O) with a free energy of -0.96 eV. This is expected to boost proton transfer for the hydrogenation of N₂ adsorbed on adjacent Sm sites. As a result, the reaction kinetics of

ENRR on S-Sm(OH)₃(V_O) can be remarkably enhanced compared to pure Sm(OH)₃. The total density of states (TDOS) of Sm in Sm(OH)₃ and S-Sm(OH)₃(V_O) were also studied. Note that the S-Sm(OH)₃(V_O) possesses a significantly increased TDOS above the Fermi level compared to Sm(OH)₃ (Figure 6e), suggesting a higher electrical conductivity.^[39] The charge-density difference of *N–NH was calculated and provided in Figure 6f. The electron transfer from S-Sm(OH)₃(V_O) to *N–NH is 0.306 |e|, markedly higher than that of Sm(OH)₃ (0.034 |e|), indicating a more robust electron interaction between S-Sm(OH)₃(V_O) and the *N–NH intermediate.^[40]

3. Conclusion

In summary, we have demonstrated greatly enhanced ENRR of Sm(OH)₃ by taking advantage of S doping and introduction of V_O. The as-obtained S-Sm(OH)₃(V_O) efficiently promoted electrochemical N₂ fixation, imparting both impressive NH₃ FE (≈29.2%) and NH₃ production rate (≈21.1 μg_{NH₃} h⁻¹ mg_{cat.}⁻¹) at an applied potential of -0.3 V. Equally importantly, over 93% of the original NH₃ yield rate and 88% of NH₃ FE were retained even after 55 h of continuous operation. DFT calculations revealed that the ENRR on S-Sm(OH)₃(V_O) tended to proceed via an alternating pathway with the formation of *N–NH intermediates (*N₂ + (H⁺ + e⁻) → *N–NH) as the PDS. The synergy induced by the combination of S dopants and V_O led to a substantial decrease in free energy of the PDS, contributing to the enhanced ENRR. The free energy change at PDS on S-Sm(OH)₃(V_O) (0.7 eV) was calculated to compare favorably with the values (≈ 1.0 eV) at the top of the ENRR volcanoes on leading transition metal surfaces. In addition, the S sites largely improved the adsorption of *H, conducive to N₂ hydrogenation, thereby accelerating the reaction kinetics of ENRR. This work provides a new perspective on the design and construction of efficient and robust electrocatalysts for NH₃ synthesis.

Supporting Information

Supporting Information is available from the Wiley Online Library or from the author.

Acknowledgements

Z. Lv and Z. Li contributed equally to this work. This work was supported by the National Natural Science Foundation of China (grant nos. 21972010 and 22022503) and Beijing Natural Science Foundation (grant no. 2192039). The name of author Hong Liu was corrected to Honghong Liu on 29 June 2023, after initial online publication of the Version of Record.

Conflict of Interest

The authors declare no conflict of interest.

Data Availability Statement

The data that support the findings of this study are available from the corresponding author upon reasonable request.

Keywords

doping, electrocatalysis, N₂ reduction, NH₃, oxygen vacancies, sulfur

Received: May 5, 2023

Revised: June 6, 2023

Published online: June 20, 2023

- [1] J. W. Erisman, M. A. Sutton, J. Galloway, Z. Klimont, W. Winiwarter, *Nat. Geosci.* **2008**, *1*, 636.
- [2] J. N. Galloway, A. R. Townsend, J. W. Erisman, M. Bekunda, Z. Cai, J. R. Freney, L. A. Martinelli, S. P. Seitzinger, M. A. Sutton, *Science* **2008**, *320*, 889.
- [3] R. Li, K. Xiang, Z. Liu, Z. Peng, Y. Zou, S. Wang, *Adv. Funct. Mater.* **2022**, *32*, 2208212.
- [4] J. Liang, Q. Liu, A. A. Alshehri, X. Sun, *Nano Res. Energy* **2022**, *1*, e9120010.
- [5] G. Soloveichik, *Nat. Catal.* **2019**, *2*, 377.
- [6] Q. Li, Y.-C. Wang, J. Zeng, X. Zhao, C. Chen, Q.-M. Wu, L.-M. Chen, Z.-Y. Chen, Y.-P. Lei, *Rare Met.* **2021**, *40*, 3442.
- [7] C.-H. Yang, F. Nosheen, Z.-C. Zhang, *Rare Met.* **2021**, *40*, 1412.
- [8] X. Zhao, G. Hu, G.-F. Chen, H. Zhang, S. Zhang, H. Wang, *Adv. Mater.* **2021**, *33*, 2007650.
- [9] G. Qing, R. Ghazfar, S. T. Jackowski, F. Habibzadeh, M. M. Ashtiani, C.-P. Chen, M. R. Smith, T. W. Hamann, *Chem. Rev.* **2020**, *120*, 5437.
- [10] H.-P. Jia, E. A. Quadrelli, *Chem. Soc. Rev.* **2014**, *43*, 547.
- [11] Q. Liu, Y. Lin, S. Gu, Z. Cheng, L. Xie, S. Sun, L. Zhang, Y. Luo, A. A. Alshehri, M. S. Hamdy, Q. Kong, J. Wang, X. Sun, *Nano Res.* **2022**, *15*, 7134.
- [12] Z. Zhao, J. Park, C. Choi, S. Hong, X. Hui, H. Zhang, T. W. B. Lo, A. W. Robertson, Z. Lv, Y. Jung, Z. Sun, *Innovation* **2022**, *3*, 100190.
- [13] M. A. Shipman, M. D. Szymes, *Catal. Today* **2017**, *286*, 57.
- [14] Y. Sun, Y. Wang, H. Li, W. Zhang, X.-M. Song, D.-M. Feng, X. Sun, B. Jia, H. Mao, T. Ma, *J. Energy Chem.* **2021**, *62*, 51.
- [15] X. Cui, C. Tang, Q. Zhang, *Adv. Energy Mater.* **2018**, *8*, 1800369.
- [16] Z. Yao, S. Liu, H. Liu, Y. Ruan, S. Hong, T.-S. Wu, L. Hao, Y.-L. Soo, P. Xiong, M. M.-J. Li, A. W. Robertson, Q. Xia, L.-X. Ding, Z. Sun, *Adv. Funct. Mater.* **2023**, 2209843.
- [17] X. Yang, J. Nash, J. Anibal, M. Dunwell, S. Kattel, E. Stavitski, K. Attenkofer, J. G. Chen, Y. Yan, B. Xu, *J. Am. Chem. Soc.* **2018**, *140*, 13387.
- [18] H. Shen, C. Choi, J. Masa, X. Li, J. Qiu, Y. Jung, Z. Sun, *Chem* **2021**, *7*, 1708.
- [19] Y. Ren, C. Yu, X. Tan, H. Huang, Q. Wei, J. Qiu, *Energy Environ. Sci.* **2021**, *14*, 1176.
- [20] L. Li, C. Tang, H. Jin, K. Davey, S.-Z. Qiao, *Chem* **2021**, *7*, 3232.
- [21] Y. Jiao, Y. Zheng, K. Davey, S.-Z. Qiao, *Nat. Energy* **2016**, *1*, 16130.
- [22] Y. Abghoui, A. L. Garden, V. F. Hlynsson, S. Björgvinsdóttir, H. Ólafsdóttir, E. Skúlason, *Phys. Chem. Chem. Phys.* **2015**, *17*, 4909.
- [23] L. Shi, Y. Yin, S. Wang, H. Sun, *ACS Catal.* **2020**, *10*, 6870.
- [24] E. Skúlason, T. Bligaard, S. Gudmundsdóttir, F. Studt, J. Rossmeisl, F. Abild-Pedersen, T. Vegge, H. Jónsson, J. K. Nørskov, *Phys. Chem. Chem. Phys.* **2012**, *14*, 1235.
- [25] Y. Li, T. Li, X. Zhu, A. A. Alshehri, K. A. Alzahrani, S. Lu, X. Sun, *Chem. Asian J.* **2020**, *15*, 487.
- [26] Z. Ma, T. Zhang, C. Jiang, *Chem. Eng. J.* **2015**, *264*, 610.
- [27] H. Jianfeng, W. Dan, Y. Lixiong, C. Liyun, O. Haibo, L. Jiayin, H. Wei, *J. Alloys Compd.* **2014**, *612*, 233.
- [28] J.-G. Kang, B.-K. Min, Y. Sohn, *J. Mater. Sci.* **2015**, *50*, 1958.
- [29] T.-D. Nguyen, D. Mrabet, T.-O. Do, *J. Phys. Chem. C* **2008**, *112*, 15226.
- [30] B. Fan, H. Wang, H. Zhang, Y. Song, X. Zheng, C. Li, Y. Tan, X. Han, Y. Deng, W. Hu, *Adv. Funct. Mater.* **2022**, *32*, 2110783.

- [31] Y. Zhao, F. Li, W. Li, Y. Li, C. Liu, Z. Zhao, Y. Shan, Y. Ji, L. Sun, *Angew. Chem. Int. Ed.* **2021**, *60*, 20331.
- [32] X. Zhang, L. Liu, A. Wu, J. Zhu, R. Si, J. Guo, R. Chen, Q. Jiang, X. Ju, J. Feng, Z. Xiong, T. He, P. Chen, *ACS Catal.* **2022**, *12*, 2178.
- [33] Q. Li, C. Fang, Z. Yang, B. Yu, M. Takabatake, K. Motokura, X. Sun, Y. Yang, *Small* **2022**, *18*, 2201343.
- [34] G.-F. Chen, Y. Yuan, H. Jiang, S.-Y. Ren, L.-X. Ding, L. Ma, T. Wu, J. Lu, H. Wang, *Nat. Energy* **2020**, *5*, 605.
- [35] Y. Gao, Q. Xia, L. Hao, A. W. Robertson, Z. Sun, *ACS Sustainable Chem. Eng.* **2022**, *10*, 1316.
- [36] D. Philip, A. Eapen, G. Aruldas, *J. Solid State Chem.* **1995**, *116*, 217.
- [37] E. Skúlason, T. Bliigaard, S. Gudmundsdottir, F. Studt, J. Rossmeisl, F. Abild-Pedersen, T. Vegge, H. Jonsson, J. K. Nørskov, *Phys. Chem. Chem. Phys.* **2012**, *14*, 1235.
- [38] Y. Kong, L. Wu, X. Yang, Y. Li, S. Zheng, B. Yang, Z. Li, Q. Zhang, S. Zhou, L. Lei, G. Wu, Y. Hou, *Adv. Funct. Mater.* **2022**, *32*, 2205409.
- [39] L. Zhang, W. Cai, N. Bao, *Adv. Mater.* **2021**, *33*, 2100745.
- [40] X. Ren, J. Zhao, Q. Wei, Y. Ma, H. Guo, Q. Liu, Y. Wang, G. Cui, A. M. Asiri, B. Li, B. Tang, X. Sun, *ACS Cent. Sci.* **2019**, *5*, 116.